INTERNATIONAL JOURNAL OF CLIMATOLOGY
Int. J. Climatol. (2017)
Published online in Wiley Online Library
(wileyonlinelibrary.com) DOI: 10.1002/joc.5049

RMetS
Royal Meteorological Society

Seasonal and intraseasonal variability of precipitable water vapour in the Chajnantor plateau, Chile

Julio C. Marín[a,c]* and Bradford S. Barrett[b]
[a] *Departamento de Meteorología, Universidad de Valparaíso, Chile*
[b] *Oceanography Department, US Naval Academy, Annapolis, MD, USA*
[c] *Centro interdisciplinario de Estudios Atmosféricos y AStroestadística (CEAAS), Universidad de Valparaíso, Chile*

ABSTRACT: The Chajnantor plateau is located in the Atacama Desert at over 4800 m above sea level. The plateau features a large fraction of days during the year where dry and stable atmospheric conditions predominate. The suitability of the type of astronomy observations routinely made at sites across the Chajnantor region at different times of the year depends on the variability of atmospheric water vapour.

In this work, we study seasonal and intraseasonal variability associated with periods of large and low precipitable water vapour (PWV) in the Chajnantor region over 32 years. We establish large-scale conditions favourable for above- and below-normal PWV for each of the four seasons. We also explore whether intraseasonal PWV variations are related to the Madden–Julian Oscillation (MJO). Below-normal PWV in winter, spring, and autumn seasons was found associated with mostly zonal 500-hPa winds, which advect drier than normal air from the anticyclone over the eastern portions of the southeast (SE) Pacific Ocean. In summer, periods with below-normal PWV were found to have anomalously south-westerly winds at mid-levels, also indicating transport of anomalously dry air from the stable SE Pacific. In winter, spring, and autumn seasons, above-normal PWV was generally associated with north-westerly mid-tropospheric wind anomalies, indicating advection of above-normal PWV from the subtropical and tropical regions of the SE Pacific Ocean. Above-normal PWV conditions in summer were associated with nearly calm winds at 500 hPa. Months and phases of the MJO for the most extreme anomalies of PWV for each season agreed well with the seasonal anomalies. Furthermore, three independent reanalysis data sets generally agreed on MJO phases associated with largest positive and negative PWV anomalies. This agreement provides evidence for the first time that the MJO modulates the PWV content over the Atacama Desert.

KEY WORDS Chajnantor plateau; PWV variability; MJO

Received 26 May 2015; Revised 11 January 2017; Accepted 2 February 2017

1. Introduction

The Atacama Desert in northern Chile is an extremely arid place that has been labelled as the driest desert on Earth, with even Mars-like soil aridity (Navarro-González *et al.*, 2003). It covers approximately 1000 km in the north–south direction (17°–25°S) and is bounded by the Andes Cordillera to the east and the Pacific Ocean to the west. The arid climate of the Atacama Desert is attributable to two factors. First, the Andes Cordillera to the east blocks the transport of humid air from the interior of the continent (Lenters and Cook, 1995; Rutllant *et al.*, 2003; Insel *et al.*, 2010). Second, the permanent subtropical southeast (SE) Pacific anticyclone is maintained by slow adiabatic subsidence from the downward branch of the Hadley cell (Rodwell and Hoskins, 2001). This SE Pacific anticyclone circulation induces southerly winds along the coast of Chile, causing the advection of colder waters from the south and the upwelling of deeper cold waters due to the wind stress on the sea surface. Warm and dry air aloft due to adiabatic compression and cold and moist air in the marine boundary layer generates a thermal inversion that is usually capped by stratus clouds (Bretherton *et al.*, 2004; Comstock *et al.*, 2005; Hannay *et al.*, 2009). These dry and stable conditions inhibit deep convective development over the ocean and, in conjunction with steep mountains slopes along the coast, prevent the flow of humid air from the ocean to the continent (Rutllant *et al.*, 2003).

The Chajnantor plateau is located in the Atacama Desert at over 4800 m above sea level, centred about 20 km from the Bolivia border and 80 km from the Argentina border (Figure 1). The plateau features a large fraction of days during the year where dry and stable atmospheric conditions predominate (Giovanelli *et al.*, 2001; Peterson *et al.*, 2003; Radford, 2011; Marín *et al.*, 2015; Rondanelli *et al.*, 2015). For this reason, a number of telescopes that operate at the submillimetre and millimetre range have been installed there [e.g. the Atacama Large Millimeter Array (ALMA; Brown *et al.*, 2004, located at 23.03°S/67.75°W) and the Atacama Pathfinder Experiment (APEX; Güsten *et al.*, 2006)]. The dry conditions in this region offer one of the best atmospheric transparencies. For example, the

* Correspondence to: J. C. Marín, Departamento de Meteorología, Universidad de Valparaíso, Av. Gran Bretaña 644, Playa Ancha, Valparaíso, Chile. E-mail: julio.marin@meteo.uv.cl

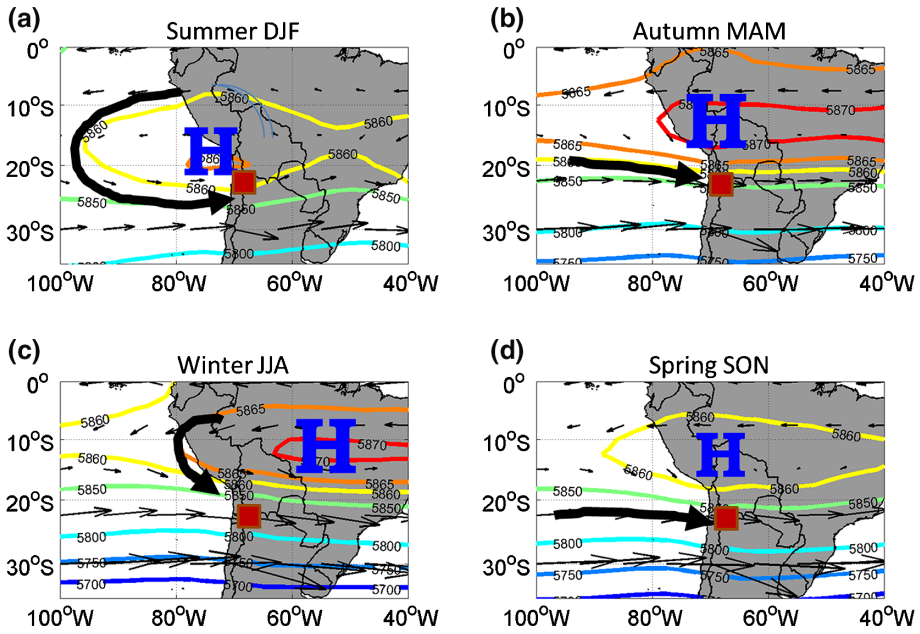

Figure 1. Seasonal mean climatology of 500-hPa height (coloured lines; in m) and winds (arrows) for 1979–2010. Maximum height (H) and representative streamlines (dark black line) for the Chajnantor region (red square) have been annotated in each season. [Colour figure can be viewed at wileyonlinelibrary.com].

ALMA telescope is equipped to observe at frequencies above 600 GHz when the precipitable water vapour (PWV) is below 1 mm. On the other hand, the atmosphere is sufficiently transparent below 380 GHz for PWV values below 2 mm and operations are feasible at frequencies below 300 GHz for PWV <5 mm (Sarazin *et al.*, 2013). At high altitudes and dry conditions, such as those of the Chajnantor plateau, the suitability of observations at different times of the year depends on the variability of atmospheric water vapour (Giovanelli *et al.*, 2001; Peterson *et al.*, 2003; Radford, 2011; Tremblin *et al.*, 2012).

The annual variation of PWV in the Chajnantor region is controlled by the large-scale atmospheric circulation. Middle- and upper-tropospheric westerly winds predominate from May to October (Figure 1) and are linked to the northward displacement of the subtropical westerly jet stream, which brings dry mid-troposphere air to the region, favouring clear skies and stable atmospheric conditions. The circulation anomalies during these months are mainly due to transient midlatitude disturbances embedded in the mean westerly flow (Garreaud *et al.*, 2003; Garreaud, 2009), which seems to be related to short periods of above-normal PWV values (Marín *et al.*, 2013, 2015). In summer months (December–February), low-latitude easterly winds extend southward associated with a westward and southward displacement of the mean anticyclone (Figure 1), reaching latitudes poleward of 20°S, and these winds are associated with thunderstorm formation (Garreaud, 2009). Low PWV values predominate during winter and spring months from May to October (which is the best period for submillimetre observations), whereas larger values are mainly found during summer months of December to February (Figure 2). Despite these studies of circulation variability, to our knowledge, there are no

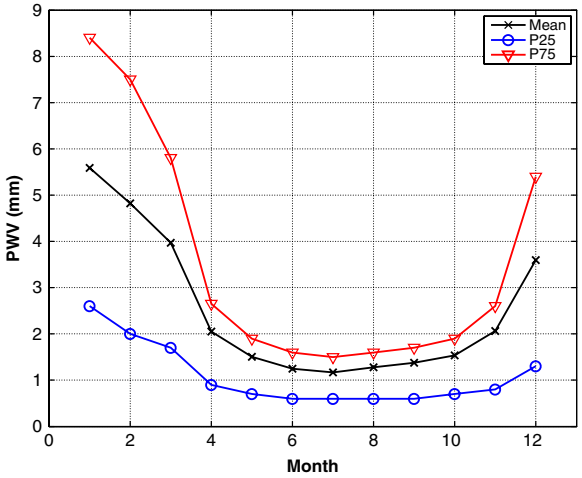

Figure 2. Monthly mean PWV in mm at the APEX site in the Chilean Atacama Desert averaged over the period 1979–2010 and the 25th and 75th percentiles used to select periods of low and high PWV. PWV values were taken from the nearest CFSR grid-point to the APEX site and are for the period 1979–2010. [Colour figure can be viewed at wileyonlinelibrary.com].

studies that have comprehensively examined the synoptic patterns associated with the seasonal variations of PWV over the Chajnantor region. Furthermore, the intraseasonal variability of PWV has not yet received attention, despite studies showing intraseasonal variability of circulation and precipitation in Chile (Jones and Carvalho, 2002; Carvalho *et al.*, 2004; Barrett *et al.*, 2012a).

As the leading mode of atmospheric intraseasonal variability, the Madden–Julian Oscillation (MJO; Madden and Julian, 1971, 1972) is seen as a coherent circulation anomaly favouring deep convection and associated

heavy precipitation that moves to the east around the Tropics with a periodicity of 30–60 days. The convectively active region typically extends to 10 000 km, and is bounded on the east and west by regions of suppressed convection and sparse precipitation (Madden and Julian, 1994). A number of studies have shown the interaction of convective heating like that of the MJO with the extratropics (Hoskins and Karoly, 1981; Mechoso *et al.*, 1991; Berbery *et al.*, 1992), and Hoskins and Karoly (1981) and Sardeshmukh and Hoskins (1988) found that this heating modulates extratropical Rossby wave activity. The MJO's influence thus extends to South America, where it affects the large-scale circulation. Barrett *et al.* (2012a) found winter-season 500-hPa height anomalies as large as 50 m, depending on the phase of the MJO. These anomalies were found responsible for observed precipitation anomalies, including statistically significant anomalies over the high-elevation regions of northern Chile. In addition, Barrett *et al.* (2012b) found that maximum daily lower-troposphere O_3 concentrations in Santiago (33°S), as well as its diurnal cycle, are also affected by the MJO through its modification of large-scale atmospheric circulation features. Juliá *et al.* (2012) found a relationship between the precipitation in north-central Chile and the MJO, although their study was more limited and they found a high rate of false alarms. Given its effects on South American atmospheric circulation, it is likely that the MJO also modulates the PWV variability over the Chajnantor region. National and regional forecast centres currently produce operational ensemble predictions of the phase and amplitude of the MJO (Rashid *et al.*, 2011; Wang, 2011), thus increasing the usefulness of statistical studies such as this one in the arena of intraseasonal prediction. The hypothesis that PWV would vary by active MJO phase was tested in this study.

The main objectives of this paper were (1) to study the synoptic patterns associated with periods of large and low PWV in the Chajnantor region over 32 years, and (2) to test whether intraseasonal PWV variations are related to the phase of the MJO. The remainder of this article is organized as follows: Section 2 describes the observations and reanalysis data used in this study and the methodologies used to select periods of low and high PWV and to relate the MJO phases to the PWV. Section 3 presents the results of the seasonal and intraseasonal PWV analysis, and a discussion of results and conclusions are presented in Section 4.

2. Data and methodology

2.1. The APEX radiometer

The APEX is a radio telescope located in the Chajnantor plateau (23.006°S, 67.759°W). This telescope is an ALMA prototype antenna designed to work at submillimetre wavelengths. There is a low humidity and temperature profiling (LHATPRO) microwave radiometer (Rose *et al.*, 2005) installed at APEX that was developed by Radiometer Physics GmbH. It takes measurements at 183.31 GHz, the frequency of the strong $3_{1,3} \rightarrow 2_{2,0}$ emission line from H_2O (Pardo *et al.*, 1996). The humidity instrument has been shown to perform very well in low-PWV environments (e.g. Ricaud *et al.*, 2010), making it a good candidate to sample PWV for telescope sites (e.g. Kerber *et al.*, 2014). The PWV data from the APEX radiometer is used in this study to show the validity of the reanalysis data over the Chajnantor region, and the remainder of the analysis of this article is then based on the reanalysis data.

2.2. The CFSR, ERA-Interim, and JRA-55 reanalyses

The primary reanalysis tool used in this study, the Climate Forecast System Reanalysis (CFSR, Saha *et al.*, 2010), is a global reanalysis created by the National Centers for Environmental Prediction (NCEP). It covers the period 1979–2010; after that, a second version was created to cover from 2011 until present. The 500-hPa geopotential height, the 500-hPa wind components, and the PWV from CFSR data at $0.5° \times 0.5°$ horizontal resolution every 6 h were used in this study for the period January 1979 to December 2010 (32 years). To use CFSR PWV to analyse synoptic patterns associated with periods of high and low PWV over the Chajnantor plateau from 1979 to 2010, the first step was to confirm that PWV from the CFSR represented reasonably well the observations over the region. PWV observations from the APEX radiometer are available from May 2006 until present. Thus, we compared the PWV from the CFSR data with observations from May 2006 to December 2010. The PWV from the CFSR was chosen at the nearest grid-point to the APEX site (67.5°W, 23°S), located a distance of about 26.5 km from the observatory and at an elevation of 4651 m. PWV was also examined in two other high-quality atmospheric reanalysis data sets, the European Center for Medium-Range Weather Forecasts (ECMWF) interim reanalysis (ERA-Interim; Dee *et al.*, 2011) and the Japanese 55-year reanalysis (JRA-55; Kobayashi *et al.*, 2015). The nearest ERA-Interim grid-point to the observatory was located at 67.5°W, 23°S at an elevation of 4265 m, while the nearest JRA-55 grid-point was at 67.5°W, 22.7°S at an elevation of 4561 m.

During the year, PWV increases during the austral summer months and it decreases during winter and spring months (Figure 2). Daily mean PWV from the CFSR reanalysis represented this observed daily mean PWV evolution over the validation period reasonably well. For example, Figure 3 shows that CFSR mainly overestimated observations for PWV values above 2 mm. The mean bias [calculated as $\sum(\mathrm{PWV_{CFSR}} - \mathrm{PWV_{APEX}})/n$] for this PWV range was +0.93 mm. Below 2 mm, the mean bias was +0.2 mm, indicating that CFSR also overestimated PWV at low values. CFSR showed a larger scatter in summer and larger overestimation of observations (Figure 3(a)). The linear correlation between CFSR and APEX observations was 0.8 in those seasons, supporting the use of CFSR in this study to account for the PWV seasonal and intraseasonal variations in the Chajnantor region. During winter, the r^2 of the fitted regression line increased to 0.79 and

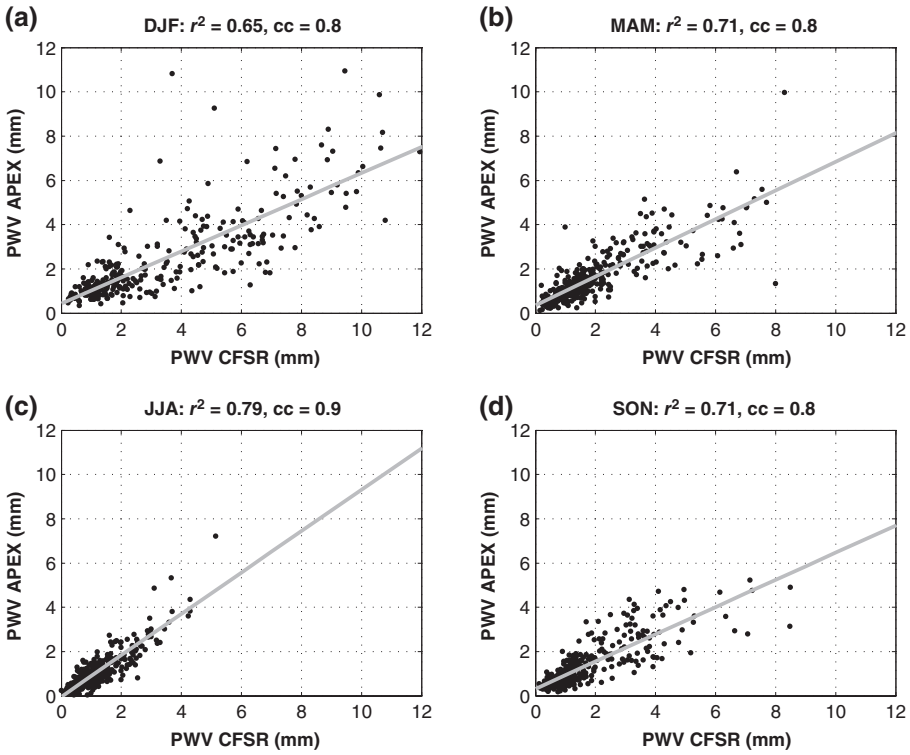

Figure 3. Scatter plot of daily mean PWV from the APEX radiometer and the CFSR grid-point closest to the APEX site, from May 2006 to December 2010, for (a) summer, (b) fall, (c) winter, and (d) spring. The r^2 and linear CC is given for data shown in each panel.

the linear correlation between CFSR and APEX increased to 0.9, showing that the correlation was better during this season when there are fewer large PWV values. Sometimes CFSR represented the observed PWV value very well, but most of the time, it overestimated it, primarily during summer. However, during winter, when the PWV is typically low, the agreement between CFSR and APEX is the best as will be discussed below.

To further examine the relationship between CFSR reanalysis and observed APEX PWV, monthly values of mean bias, root mean square error (RMSE), and correlation coefficient (CC) between the APEX radiometer and CFSR were calculated for the period when both data sets were available (May 2006 to December 2010; Figure 4). The monthly mean bias and RMSE ranged from 1.5 to 2.5 mm in summer but decreased to below 0.5 mm from May to October. Figures 2 and 3 indicate that CFSR overestimated PWV when it increases during summer months, but for low PWV values, which typically occur from fall to spring, the absolute error and bias decreased. These differences could be due to both differences between elevation between the CFSR grid-point and the APEX observatory and also the size of CFSR grid (at 0.5° spacing, the grid is approximately 50 km × 50 km). Nevertheless, the CFSR was strongly linearly correlated with the observations, with CCs between 0.75 and 0.85 most of the year, except March and December, when CCs decreased to 0.62 and 0.73, respectively (Figure 4).

Since the Chajnantor plateau is located over 4800 m above sea level, circulation and height on the 500-hPa pressure surface were composited to study both the

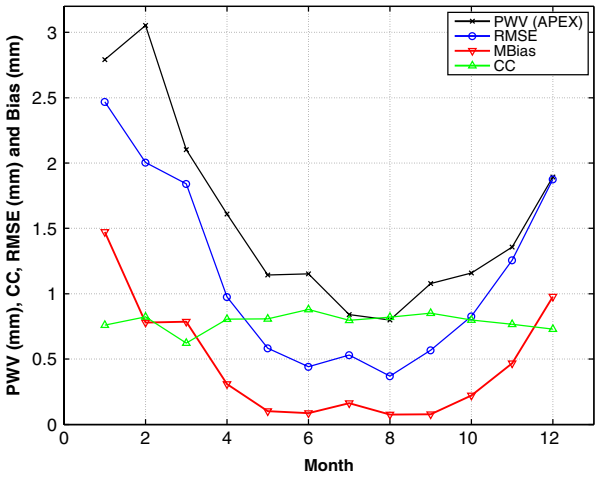

Figure 4. Monthly mean PWV from the APEX radiometer, and monthly mean bias, RMSE and CC between APEX observations and the CFSR reanalysis, all for the period May 2006 to December 2010. [Colour figure can be viewed at wileyonlinelibrary.com].

middle-atmosphere synoptic patterns associated with periods of low and high PWV in the region and the anomalous synoptic patterns associated with different phases of the MJO. To select days with high and low PWV in the Chajnantor plateau, we used the PWV from the CFSR grid-point nearest to the APEX site. The PWV was also used to calculate monthly mean PWV values, which were then used to examine the annual cycle (Figure 2). For each season, times when the averaged PWV was larger than the 75th percentile, and times when the averaged PWV

was less than the 25th percentile, were classified as high and low PWV episodes, respectively, for that season. As Figure 2 shows, the 25th and 75th percentiles increased during summer months compared to the other months, justifying their use instead of fixed threshold values over the year to select periods of low and high PWV values. Days with PWV above the 75th percentile, and days with PWV below the 25th percentile, were then used to calculate composite means of the synoptic-scale environment for high and low PWV episodes, respectively. Finally, both 500- and 250-hPa height and wind fields were composited for those same days to analyse the synoptic patterns associated with periods of high and low PWV over the Chajnantor plateau. Since the results at mid- and upper-troposphere (500 and 250 hPa, respectively) were similar, only the variability at 500 hPa is presented here.

2.3. Method to diagnose the MJO

Daily averaged PWV values from CFSR over the Chajnantor plateau were sorted by active phase of the MJO using the real-time multivariate MJO (RMM) index of Wheeler and Hendon (2004) with interannual variability removed. Active MJO days were defined where RMM amplitude was >1.0. Longitudinal bands corresponding to regions of active tropical convection are represented by eight MJO phases according to Wheeler and Hendon (2004). Mean daily PWV values for each of the eight RMM MJO phases were then calculated for each month, for the period 1979–2010. Anomalous PWV values were calculated by subtracting mean monthly PWV (for all days in the month, regardless of MJO activity or phase) from the daily mean PWV for each MJO phase. Percent values of normal were then calculated by dividing each anomaly value by the monthly mean. To identify and understand physical mechanisms behind the most significant intraseasonal variability at Chajnantor in each month, the MJO phases associated with the largest positive and negative PWV anomalies were selected. Furthermore, to narrow the focus to the most extreme events, as those are of most interest to the ALMA and APEX operations, only the largest positive and negative months for each season were selected for further study. For those selected months, composite anomalies of CFSR 500-hPa height, 500-hPa u- and v-wind components, and PWV were calculated for each active MJO phase. Those anomalies were calculated by subtracting monthly mean values of all days from monthly mean values for only that active MJO phase, following the methodology of Barrett *et al.* (2012a, 2012b). To test PWV anomalies of each phase for statistical significance, they were compared to monthly means and standard deviations. Using the Student's t-test, anomalies that were significant at the 90% confidence interval (p-value of 0.10) were retained.

2.4. The MJO as an aid to predict PWV

Perhaps the most useful application of the results in this study to PWV forecasting is the ability to identify possible episodes of below- and above-normal PWV beyond the typical skill of a numerical weather prediction (NWP) model (5–7 days; Bauer *et al.*, 2015). The MJO is one of the sources of extratropical variability, manifested as a modulation of atmospheric Rossby waves (Madden and Julian, 1994; Cassou, 2008), including in the Southern Hemisphere (Barrett *et al.*, 2012a, 2012b; Flatau and Kim, 2013; Fauchereau *et al.*, 2016). As PWV variability in the Chajnantor region is related to atmospheric circulation and Rossby wave activity (Falvey and Garreaud, 2005), linking PWV to the MJO may extend PWV predictability and be useful to operational scheduling at the site, particularly given that forecasts of PWV from the Global Forecast System (GFS) model drop below skill (correlation) of 0.7 after about 120 h (Sarazin *et al.*, 2013). The MJO has shown statistically significant predictability in global NWP models well beyond 120 h. For example, prediction skill of the RMM indices of approximately 21 days (Kim *et al.*, 2014) was found in the Climate Forecast System version 2 (CFSv2), of 3–4 weeks (Xiang *et al.*, 2015) in the Geophysical Fluid Dynamics Laboratory (GFDL) model, of 27 days (Miyakawa *et al.*, 2014) in the Nonhydrostatic Icosahedral Atmospheric Model (NICAM), and of 16–17 days (Wu *et al.*, 2016) in an ensemble of the Beijing Climate Center Atmospheric General Circulation Model. All of these studies suggest that the tropical MJO can act as an effective bridge into subseasonal prediction of extratropical atmospheric events (Jones, 2015), including PWV amounts in the Chajnantor region. The Australian Bureau of Meteorology maintains a web page with real-time analysis of the current state of the MJO, including current phase and amplitude of the Wheeler and Hendon (2004) RMM index (http://www.bom.gov.au/climate/mjo/), where observatory staff can check the current status of the MJO.

3. Results

3.1. Seasonal variability during periods of low and high PWV

Figure 5(a) shows the spatial distribution of mean PWV, geopotential height and wind fields at 500 hPa, averaged over the period 1979–2010 during the austral summer, for times when PWV < 25th percentile. Figure 5(c) shows the spatial distribution of anomalies from the long-term monthly mean (over the 1979–2010 period) of PWV, geopotential height and wind fields at 500 hPa, for summer months when PWV < 25th percentile. Low PWV episodes were found to occur in austral summer under the influence of anomalously strong 500-hPa south-westerly winds associated with a stronger than average cyclonic anomaly in the geopotential height, centred at about 32°S, 62°W, over northern Argentina (Figure 5(c)). The anomalous cyclonic circulation is the result of stronger westerly winds between 20° and 30°S and weaker westerly winds between 35° and 45°S. Negative PWV anomalies predominate over a large part of the continent and over the SE Pacific. These are stronger over the Chajnantor region (3–5 mm below normal), and extend over a NW–SE oriented strip. On

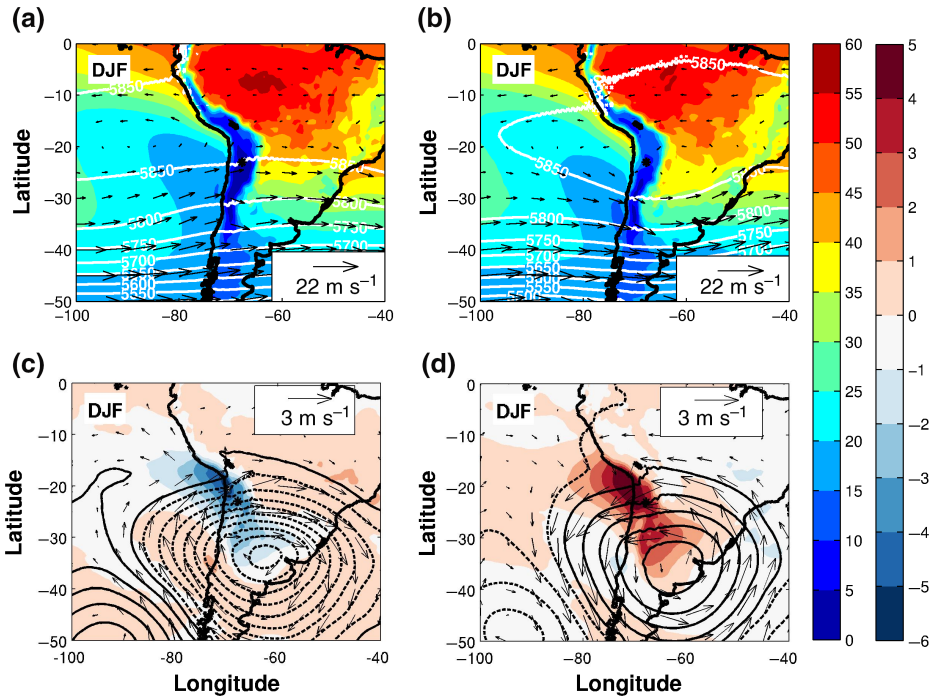

Figure 5. Mean PWV (in mm; colour shaded) and the geopotential height (in m, solid lines) and wind vectors at 500 hPa averaged over summer months (December to February) from 1979 to 2010 for (a) times when PWV < 25th percentile and (b) times when PWV > 75th percentile. PWV (in mm, colour shaded), geopotential height (negative values in dashed starting at −1 m and positive values in solid starting at 1 m, every 8 m) and wind vector anomalies at 500 hPa compared to the monthly mean (over the 1979–2010 period) during summer months for (c) times when PWV < 25th percentile and (d) times when PWV > 75th percentile. The black star shows the location of the APEX site. [Colour figure can be viewed at wileyonlinelibrary.com].

the contrary, days with PWV above the 75th percentile in summer (Figures 5(b) and (d)) are characterized by a NW–SE stripe of positive PWV anomalies that covers the Chajnantor plateau, where the highest PWV values (3–5 mm) above normal are shown (Figure 5(d)). These times show an anomalous anticyclonic circulation centred around 35°S, 60°W, which is the result of nearly calm winds at 500 hPa (seen as easterly wind anomalies in Figure 5(d)) over the continent between 15° and 30°S (Figure 1). This weaker mid-troposphere flow likely results in less transport of dry air from the subtropical SE Pacific anticyclone, a pattern identified by Vuille (1999) as favouring a southward-displaced Bolivian anticyclone and wetter conditions in the region.

Autumn months (March through May) also show the NW–SE stripe of negative PWV anomalies extending from the northern part of Chile and the adjacent oceans to the northern part of Argentina and over the Chajnantor region during days with PWV below the 25th percentile (Figure 6(c)). Zonal (westerly) flow (Figure 6(a)) with a small southerly component over northern Chile at 500 hPa is seen during periods of low PWV, and this flow is seen as anomalous southerly winds that result from anomalous anticyclonic and cyclonic circulations whose centres are located at the western and eastern edges of the continent, respectively (Figure 6(c)). The 500 hPa negative height anomalies associated with the cyclonic circulation are smaller this season than in summer. These features may advect drier air to the region from the SSW (Figure 6(a)). Autumn days with PWV above the 75th percentile over Chajnantor show the reverse synoptic pattern (Figures 6(b) and (d)). A NW–SE oriented stripe of positive PWV anomalies extends from Uruguay to the southern part of Peru and the adjacent ocean (3–5 mm above normal), covering the Chajnantor plateau. Anomalous 500-hPa cyclonic and anticyclonic circulations located in the Pacific and Atlantic oceans, respectively, result in mean troughing approximately 500 km west of Chile and north-westerly 500-hPa flow over most of northern Chile (Figure 6(c)). These anomalous features during periods of high PWV in autumn months likely advect higher PWV air to the region from lower-latitude tropical SE Pacific Ocean (Figure 6(b)).

Winter and spring months show the same features described for the autumn season but with different magnitudes for the anomalies and slightly different locations for the circulation centres (Figures 7(a)–(d) and 8(a)–(d)). In both seasons, a NW–SE strip of negative (positive) anomalies extending from the northern part of Argentina to the southern part of Peru and the adjacent Pacific Ocean is seen during periods of low (high) PWV at the Chajnantor plateau. Driving these anomalies in PWV are anomalous ridging over northern Chile and troughing over eastern Argentina and Uruguay for the case of low PWV, and anomalous troughing over northern Chile and anomalous ridging over eastern Argentina and Uruguay for the case of high PWV. These height anomaly dipoles are associated with zonal flow (Figures 7(a) and 8(a))

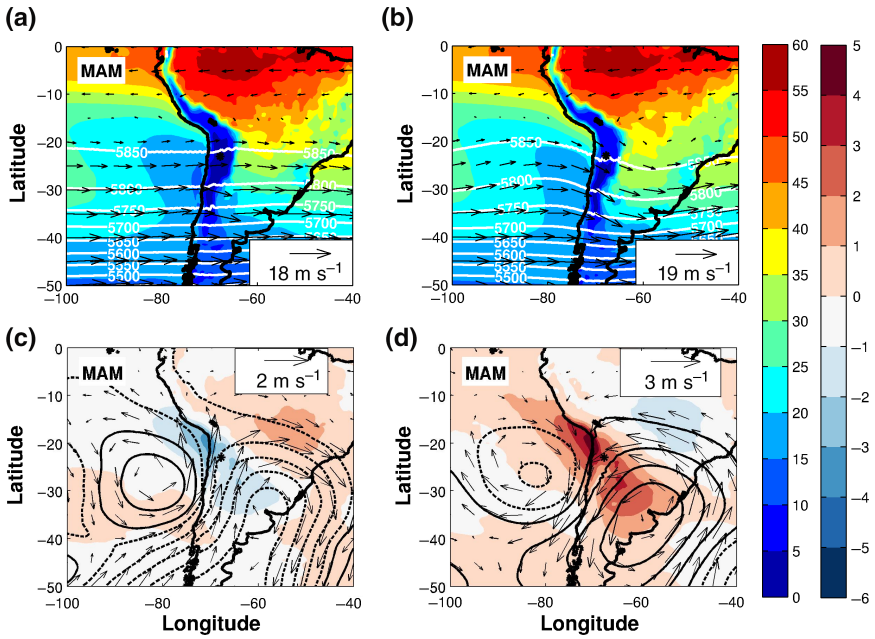

Figure 6. Same as Figure 5, but for austral fall months (March to May). [Colour figure can be viewed at wileyonlinelibrary.com].

at 500 hPa for days with low PWV or north-westerly flow (Figures 7(b) and 8(b)) at 500 hPa for days with high PWV.

3.2. PWV intraseasonal variability over the Chajnantor region

Mean daily anomalies of PWV from the CFSR were calculated for each active phase of the MJO (Figure 9(a)) and were expressed as percentage departures from the long-term (1979–2010) mean. Several important patterns emerged. First, despite a pronounced annual cycle in PWV where mean daily PWV in summer (3–6 mm) was more than double the mean daily PWV in winter (1–2 mm) (Figure 2), percent departures from normal for each month were mostly constant. For example, in all months of the year, the most negative departures from normal (indicated by diamonds in Figure 9(a)) ranged from 10 to 20% below normal. Similarly, the most positive departures from normal (indicated by circles in Figure 9(a)) mostly ranged from 15 to 30%, although in August, PWV was more than 45% above normal on days when the MJO was in phase 7, and in December, PWV was more than 35% above normal on days when the MJO was in phase 1 (Figure 9(a)). Second, several phases emerged as being most important to PWV variability in the region. For example, phase 7 was repeatedly found associated with the largest above-normal PWV values in 5 months, and phase 1 was most often associated with below-normal PWV values, also in 5 months (Table 1).

Anomalies of PWV in the JRA-55 (Figure 9(b)) and ERA-Interim (Figure 9(c)) data sets, which are independent of the CFSR, strongly supported the PWV anomalies from the CFSR data set. In 7 months (January to June and August), all three data sets agreed on the phases with the greatest positive PWV anomaly (Table 1). In the other 5 months (February, April, and October to December), two of the three data sets agreed on the phases with the highest PWV (Figures 9(a)–(c)). Furthermore, in 5 months (February, April, and October to December), all three data sets agreed on the phases with the largest negative PWV anomaly. In the other 7 months, two of the three data sets agreed on the phases with the largest negative PWV anomaly. From an operational perspective, this result means that confidence in the observed PWV anomalies by MJO phase is highest in months with agreement between all three reanalyses. Those phases are indicated by bold text in Table 1.

In general, phases 6–8 were most associated with largest positive mean PWV and phases 1–3 with largest negative mean PWV (Figure 9(a)). This relationship, with high phases leading low phases, is a result of the cyclic nature of the MJO, whereby the convective and circulation anomalies of the oscillation progress eastward (Zhang, 2005). The extratropical atmosphere responds to these convective anomalies with Rossby waves (Sardeshmukh and Hoskins, 1988; Zhang, 2013), and the atmospheric circulation anomalies produced by these Rossby waves are the physical mechanism for the observed intraseasonal PWV variability. In the next section, we examine composite anomalies of PWV and 500-hPa height and circulation for the MJO phases associated with largest, and the smallest, PWV anomalies in each season. Synoptic-scale anomaly patterns in those phases are then compared to the seasonal mean circulation patterns presented in Figures 5 and 8 for days with high and low PWV, respectively.

3.2.1. Summer

In December, days when the MJO was in phase 2 (anomalous convection over the Indian Ocean) were associated with the most negative PWV anomalies

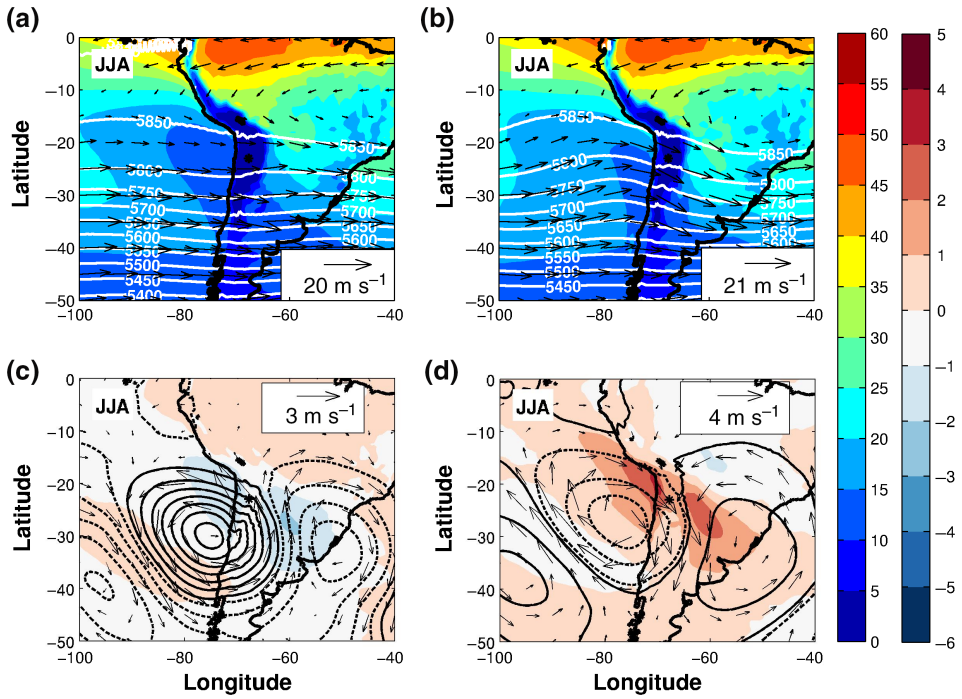

Figure 7. Same as Figure 5, but for austral winter months (June to August). [Colour figure can be viewed at wileyonlinelibrary.com].

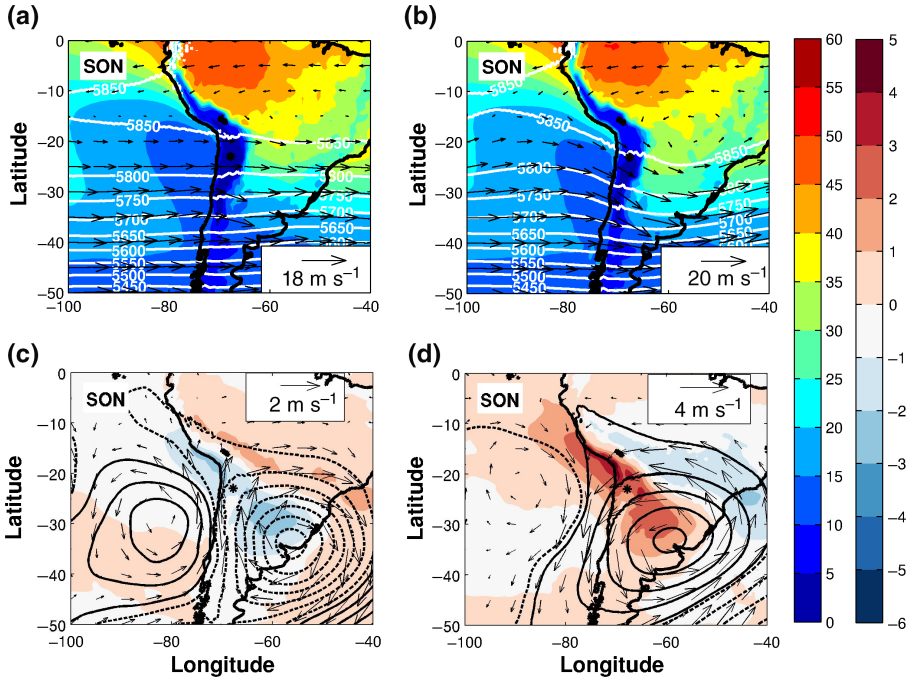

Figure 8. Same as Figure 5, but for austral spring months (September to November). [Colour figure can be viewed at wileyonlinelibrary.com].

(−0.8 mm, or 16.6% below the 1979–2010 December mean) (Figures 10(a) and (c)). On the synoptic scale, negative anomalies of PWV were mostly confined to over and to the south of the APEX site. Negative height anomalies at 500 hPa were seen over much of the SE Pacific Ocean, southern cone of South America, and southwest Atlantic Ocean, while positive 500-hPa height anomalies were seen west of Peru. Mean flow at 500 hPa during December phase 2 was zonal (Figure 10(a)) and stronger than normal (Figure 10(c)), suggesting advection of drier mid-troposphere air from the subtropical SE Pacific Ocean. This pattern of height and circulation anomalies for December phase 2 indicates that the physical mechanism by which the MJO modulated PWV during December phase 2 was via a strengthening of the zonal flow to the west of the Chajnantor region. This synoptic pattern also resembled the pattern for summer days with below-normal PWV (Figures 5(a) and (c)).

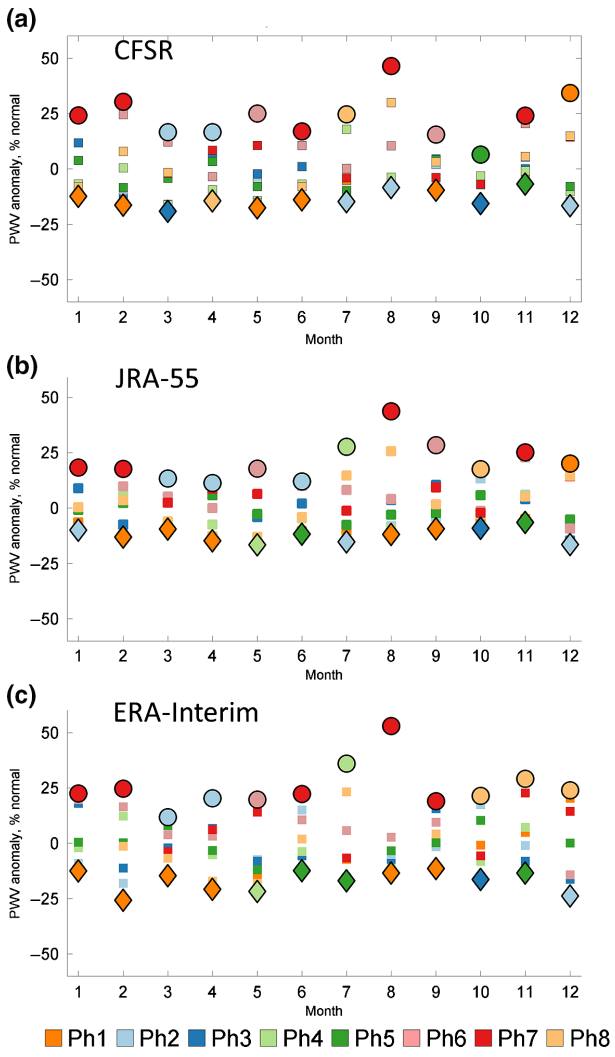

Figure 9. Mean monthly PWV anomalies (expressed as a percent of monthly mean values) for each active MJO phase for (a) CFSR, (b) JRA-55, and (c) ERA-Interim reanalyses. The two most important anomalies for each month are indicated by enlarged symbols: the largest positive anomaly for each month is indicated by a large circle and the largest negative anomaly for each month is indicated by a large diamond. All PWV data are for the respective grid points closest to the Chajnantor observatory from 1979 to 2010. [Colour figure can be viewed at wileyonlinelibrary.com].

December days when the MJO was in phase 1 (anomalous convection over Africa) were associated with the largest positive PWV anomalies in summer (+1.6 mm, or 34.3% above the 1979–2010 December mean). Synoptic-scale positive PWV anomalies were mostly confined to the Chajnantor region (Figure 10(d)). Positive height anomalies at 500 hPa were seen over a region from the Pacific Ocean west of north-central Chile east into the southwest Atlantic Ocean, while over and west of southern Chile, 500-hPa heights were below normal (Figure 10(d)). This resulted in seasonally typically weak flow speeds at 500 hPa over northern Chile (Figures 10(b) and (d)), similar to the summer pattern on days with PWV above the 75th percentile (Figures 5(b) and (d)). Physically, a stronger and southward-displaced Bolivian High, as seen in Figure 10(d), is associated with wetter conditions over the altiplano systems (Vuille, 1999).

Table 1. MJO phases with highest and lowest PWV anomalies by month. Data from CFSR point closest to the APEX site, 1979–2010. High PWV phases indicated by circles in Figure 9(a) and low PWV phases by diamonds in Figure 9(a). Bold lettering indicates unanimous agreement between CFSR, ERA-Interim, and JRA-55 reanalyses. Italics lettering indicates agreement between two of the three reanalyses.

Month	High PWV phase	Low PWV phase
January	**Phase 7**	*Phase 1*
February	**Phase 7**	**Phase 1**
March	**Phase 2**	*Phase 3*
April	**Phase 2**	**Phase 8**
May	**Phase 6**	*Phase 1*
June	**Phase 7**	*Phase 1*
July	*Phase 8*	*Phase 2*
August	**Phase 7**	*Phase 2*
September	*Phase 6*	*Phase 1*
October	*Phase 5*	**Phase 3**
November	*Phase 7*	**Phase 5**
December	*Phase 1*	**Phase 2**

3.2.2. *Autumn*

In autumn, March days in phase 3 (anomalous convection over the Indian Ocean) featured the strongest negative PWV anomalies (−1.0 mm, or 19.1% below the 1979–2010 March mean). Synoptic-scale negative PWV anomalies were seen over the Chajnantor region and northwest into the tropical SE Pacific Ocean (Figure 11(c)). Below-normal 500-hPa heights were located over much of southern South America, including the Chajnantor region, while above-normal heights were located over the Pacific Ocean to the west. This height pattern resulted in offshore 500-hPa flow over the Pacific Ocean near 10°S, 80°W, and this offshore flow reduced PWV over and to the northwest of the Chajnantor region, combined with zonal westerly flow near 25°S, resulted in reduced PWV values over and to the west of the Chajnantor region during March phase 3.

Days in May phase 6 (anomalous convection over the western Pacific) were associated with strongest positive PWV anomalies in autumn (+0.6 mm, or 25.1% above the 1979–2010 May mean) (Figures 11(b) and (d)). Positive PWV anomalies extended from the observatory site northward and eastward (Figure 11(d)), physically the result of a mean 500-hPa height field that showed troughing immediately west of Chile (Figure 11(b)) and negative height anomalies over central and northern Chile (Figure 11(d)). This height field resulted in stronger and anomalous 500-hPa flow from the northwest that advected higher PWV air to the southeast to the Chajnantor region. This flow pattern strongly resembles the composite fields (Figure 6(b)) and anomalies (Figure 6(d)) for autumn days with PWV above the 75th percentile.

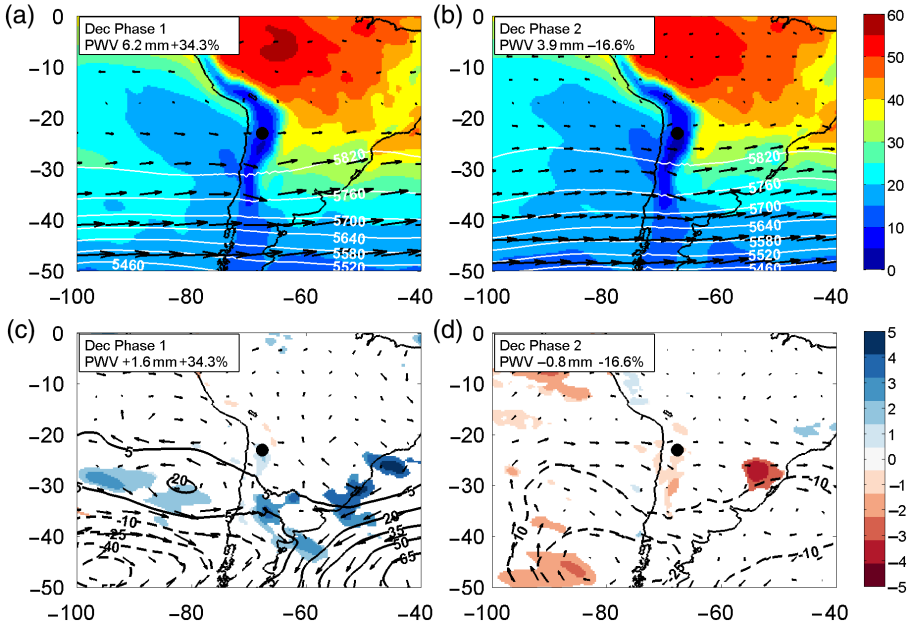

Figure 10. Daily composite means (a and b) and anomalies (departures from the monthly mean; c and d) of precipitable water (in mm; colour shaded), 500 hPa height (in m, solid and dashed lines indicate positive and negative anomalies, respectively, with 15-m contour interval), and 500 hPa wind for December phase 2 (a and c) and December phase 1 (b and d). All data are from the CFSR reanalysis over the period 1979–2010. Precipitable water anomalies are statistically significant at the 90% confidence level. [Colour figure can be viewed at wileyonlinelibrary.com].

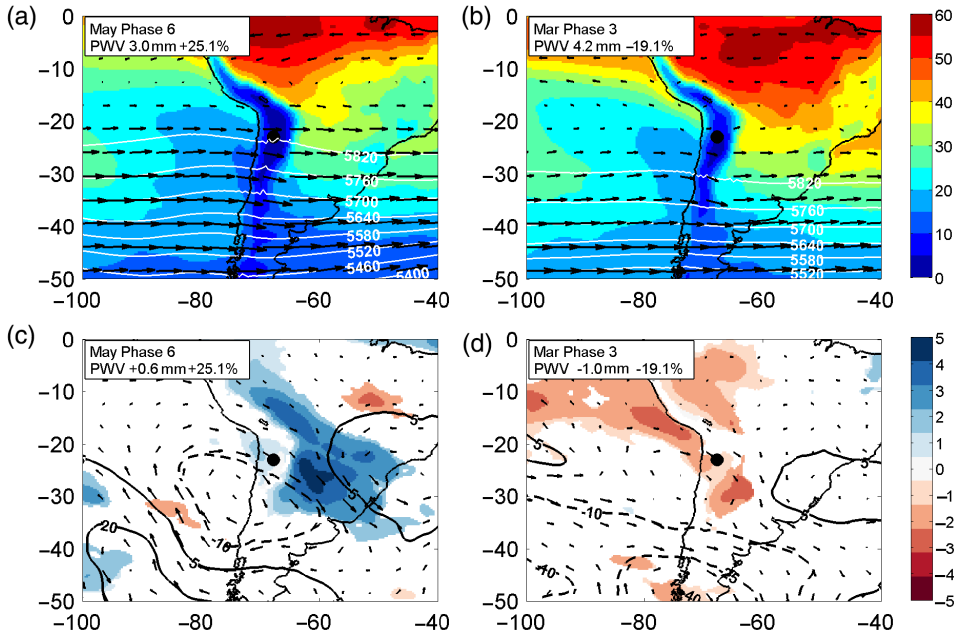

Figure 11. As in Figure 10, but for March phase 3 (a and c) and May phase 6 (b and d). [Colour figure can be viewed at wileyonlinelibrary.com].

3.2.3. *Winter*

In winter, days in July phase 2 (anomalous convection over the Indian Ocean) were associated with the strongest negative PWV anomalies over the Chajnantor region (−0.3 mm, or 14.8% below the 1979–2010 July mean). Negative PWV anomalies were confined for phase 2 to a region immediately adjacent to the observatory site (Figure 12(c)). Mean 500 heights were zonal during July phase 2 (Figure 12(a)), with negative height anomalies seen over much of Chile and adjacent Pacific Ocean waters (Figure 12(c)). Flow at 500 hPa in response to these height anomalies was anomalously strong from the west (Figure 12(c)), indicating the physical mechanism for low PWV during phase 2 in July was through advection of lower PWV air from the west.

Days in August phase 7 (anomalous convection over the western Pacific) were associated with strongest positive PWV anomalies over the Chajnantor region in winter (+0.9 mm, or 46.5% above the 1979–2010 August mean).

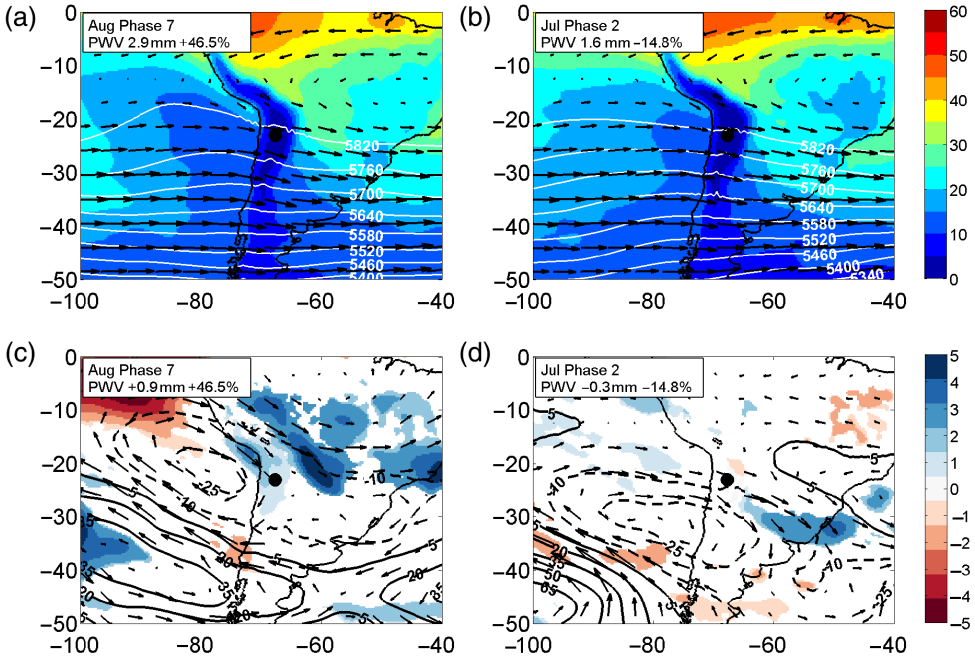

Figure 12. As in Figure 10, but for July phase 2 (a and c) and August phase 7 (b and d). [Colour figure can be viewed at wileyonlinelibrary.com].

This percent anomaly was also the largest for any month (Figure 9). During phase 7, positive PWV anomalies were located over a region including most of northern Chile and southern Peru (Figure 12(d)). These positive PWV anomalies were the result of mean 500-hPa troughing to the west of Chile and ridging over the southern SE Pacific Ocean (Figure 12(b)), resulting in mean north-westerly 500-hPa flow over the Chajnantor region. This mean north-westerly flow transported higher PWV air from the tropical SE Pacific to the ALMA and APEX observatory sites. These height and circulation anomalies during August phase 7 resembled mean height and circulation patterns and anomalies for days with PWV above the 75th percentile (Figures 7(b) and (d)).

3.2.4. Spring

In spring, October days in phase 3 (anomalous convection over the Indian Ocean) were associated with strongest negative PWV anomalies in autumn over the Chajnantor region (−0.4 mm, or 15.7% below the 1979–2010 October mean). During phase 3, regions of negative PWV anomalies were located from central Peru south into northern Argentina and Chile (Figure 13(c)), and these PWV anomalies were likely the result of reduced advection of PWV from the subtropical SE Pacific Ocean in response to 500-hPa ridging over and west of northern Chile (Figures 13(a) and (c)). Flow anomalies over the Chajnantor region were weakly southerly (Figure 13(c)), similar to the circulation patterns (Figure 8(a)) and anomalies (Figure 8(c)) for autumn days with PWV below the 25th percentile.

Days in November phase 7 (anomalous convection over the western Pacific) were associated with the strongest positive PWV anomalies over the Chajnantor region in spring (+0.7 mm, or 24.0% above the 1979–2010 November mean). Positive PWV anomalies were seen from Chajnantor south into central Chile (Figure 13(d)), physically the result of mean ridging over Argentina and weak troughing west of Chile that yielded anomalously strong west–northwest flow over the Chajnantor region (Figure 13(b)). This anomalous west-north-westerly flow would transport anomalously high PWV air from the SE Pacific to the Chajnantor region, similar to the mean flow and anomaly patterns seen on spring days with PWV above the 75th percentile (Figures 8(b) and (d)).

4. Conclusions and discussion

Precipitable water content in the Chajnantor region of northern Chile, including at the ALMA and APEX telescope sites, was found to have pronounced annual variability. Summer-season PWV values were highest, ranging from 3.5 to 6 mm in CFSR, and winter-season PWV values were lowest, ranging from 1 to 1.5 mm in CFSR. Mean atmospheric circulation anomalies also exhibited significant annual variability. Several distinct patterns emerged to explain this seasonal variability of PWV, with three seasons (autumn, winter, and spring) behaving similar to each other and different from summer. Specifically, in autumn, winter, and spring, anomalous 500-hPa ridging to the west of northern Chile and 500-hPa troughing to the east of northern Chile, accompanied by anomalous southerly 500-hPa circulation, forced mostly zonal 500-hPa flow over northern Chile. This zonal flow transported dry air eastward from the subtropical SE Pacific Ocean anticyclone to the Chajnantor region. When the height and circulation patterns reversed in autumn, winter, and spring, anomalous troughing west of northern

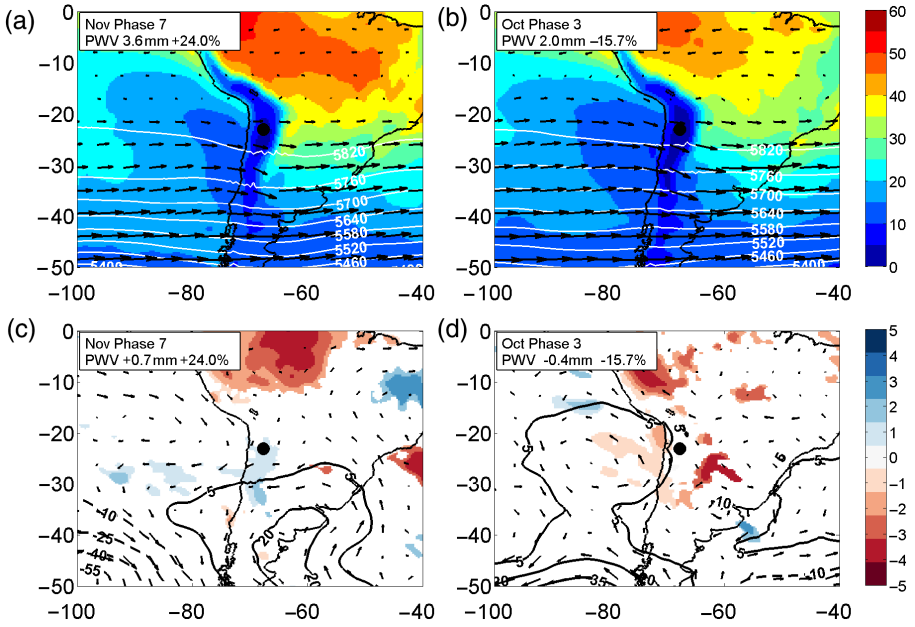

Figure 13. As in Figure 10, but for October phase 3 (a and c) and November phase 7 (b and d). [Colour figure can be viewed at wileyonlinelibrary .com].

and central Chile and anomalous ridging over Argentina were seen, accompanying anomalous north-westerly flow at 500 hPa and higher PWV values in a stripe along the Peruvian and northern Chilean coasts. This anomalous north-westerly flow acts to transport high PWV air from the tropical and subtropical SE Pacific Ocean southeastward to the Chajnantor region.

In summer (DJF), a different synoptic pattern emerged. For days with PWV below the 25th percentile, mean 500-hPa troughing was seen over central Chile and Argentina and mean ridging over northern Chile and Peru, resulting in a dry 500-hPa circulation from the southwest. For summer days with PWV above the 75th percentile, height and circulation patterns reversed periods, and positive 500-hPa height anomalies were seen over central Chile and Argentina and negative height anomalies west of Peru. This resulted in weak, to nearly calm, mean flow at 500 hPa, a synoptic pattern Vuille (1999) associated with above-normal precipitation and a southward-displaced Bolivian anticyclone.

Anomalies of PWV were also examined by MJO phase for each month. Anomalies >15% above and below monthly normal values were commonly seen in three independent reanalysis data sets. To focus on the analysis by season, composite mean and anomalies of 500-hPa heights and circulation were analysed for the MJO phases that featured the largest positive, and the largest negative, PWV anomalies for each season in the CFSR data. In general, phases 6–8 were most associated with largest positive mean PWV and phases 1–3 with largest negative mean PWV. Strongest agreement between three different reanalyses was found for above-normal PWV in January to June and August, while strongest agreement was found for below-normal PWV in February, April, and October to December. Because of that agreement, confidence in the MJO modulation of PWV is highest in those months. It is also important to note that anomalous convection in the Indian Ocean (phases 2 and 3) was associated with the most negative CFSR PWV anomalies over the Chajnantor region in every season. Similarly, anomalous convection in the western Pacific Ocean (phases 6 and 7) or Africa (phase 1) was associated with the most positive PWV anomalies in every season. This suggests that telescope operations can expect better conditions (lower PWV) when MJO is active in the Indian Ocean and poorer conditions (higher PWV) when MJO convection is active in the western Pacific. It also means that near neutral conditions might be expected in summer, autumn, and winter when MJO convection is over the Maritime Continent (phases 4 and 5), as those two phases were not associated with any monthly extremes during those seasons.

Acknowledgements

The authors acknowledge the Fondecyt project 11121473 and the Centro interdisciplinario de Estudios Atmosféricos y AStroestadística (CEAAS) of Universidad de Valparaíso for supporting this research. APEX radiometer data were provided by the APEX staff. We thank the Computational Information Systems Laboratory (CISL) Research Data Archive to provide the CFSR, ERA-Interim and JRA-55 data used in this study. We finally thank three anonymous reviewers for their many helpful comments and suggestions.

References

Barrett BS, Carrasco JF, Testino AP. 2012a. Madden–Julian Oscillation (MJO) modulation of atmospheric circulation and Chilean winter precipitation. *J. Clim.* **25**: 1678–1688.

Barrett BS, Fitzmaurice SJ, Pritchard SR. 2012b. Intraseasonal variability of surface ozone in Santiago, Chile: modulation by phase of the Madden–Julian Oscillation (MJO). *Atmos. Environ.* **55**: 55–62.
Bauer P, Thorpe A, Brunet G. 2015. The quiet revolution of numerical weather prediction. *Nature* **525**: 47–55.
Berbery EH, Nogue's-Paegle J, Horel JD. 1992. Wavelike Southern Hemisphere extratropical teleconnections. *J. Atmos. Sci.* **49**: 155–177.
Bretherton CS, Uttal T, Fairall CW, Yuter SE, Weller RA, Baumgardner D, Comstock K, Wood R, Raga GB. 2004. The epic 2001 stratocumulus study. *Bull. Am. Meteorol. Soc.* **85**: 967–977.
Brown RL, Wild W, Cunningham C. 2004. ALMA – the Atacama large millimeter array. *Adv. Space Res.* **34**: 555–559.
Carvalho L, Jones C, Liebmann B. 2004. The South Atlantic convergence zone: intensity, form, persistence, and relationships with intraseasonal to interannual activity and extreme rainfall. *J. Clim.* **17**: 88–108.
Cassou C. 2008. Intraseasonal interaction between the Madden–Julian Oscillation and the North Atlantic Oscillation. *Nature* **455**: 523–527.
Comstock KK, Bretherton CS, Yuter SE. 2005. Mesoscale variability and drizzle in southeast Pacific stratocumulus. *J. Atmos. Sci.* **62**: 3792–3807.
Dee DP, Uppala SM, Simmons AJ, Berrisford P, Poli P, Kobayashi S, Andrae U, Balmaseda MA, Balsamo G, Bauer P, Bechtold P, Beljaars ACM, van de Berg L, Bidlot J, Bormann N, Desol C, Dragani R, Fuentes M, Geer AJ, Haimberger L, Healey SB, Hersbach H, Holm EV, Isaksen L, Kallberg P, Kohler M, Matricardi M, McNally AP, Monge-Sanz BM, Morcrette JJ, Park BK, Beubey C, de Rosnay P, Tavolato C, Thepaut JN, Vitart F. 2011. The ERA-Interim reanalysis: configuration and performance of the data assimilation system. *Q. J. R. Meteorol. Soc.* **137**: 553–597.
Falvey M, Garreaud RD. 2005. Moisture variability over the South American altiplano during the South American Low Level Jet Experiment (SALLJEX) observing season. *J. Geophys. Res. Atmos.* **110**: D22105.
Fauchereau N, Pohl B, Lorrey A. 2016. Extratropical impacts of the Madden–Julian Oscillation over New Zealand from a weather regime perspective. *J. Clim.* **29**: 2161–2175.
Flatau M, Kim Y-J. 2013. Interaction between the MJO and polar circulations. *J. Clim.* **26**: 3562–3574.
Garreaud RD. 2009. The Andes climate and weather. *Adv. Geosci.* **22**: 3–11.
Garreaud R, Vuille M, Clements A. 2003. The climate of the Altiplano: observed current conditions and past change mechanisms. *Palaeogeogr. Palaeoclimatol. Palaeoecol.* **3054**: 1–18.
Giovanelli R, Darling J, Henderson C, Hoffman W, Barry D, Cordes J, Eikenberry S, Gull G, Keller L, Smith JD, Stacey G. 2001. The optical/infrared astronomical quality of high Atacama sites. II. Infrared characteristics. *Publ. Astron. Soc. Pac.* **113**: 803–813.
Güsten R, Nyman LA, Schilke P, Menten K, Cesarsky C, Booth R. 2006. The Atacama Pathfinder EXperiment (APEX) – a new submillimeter facility for the southern skies. *Astron. Astrophys.* **454**: L13–L16.
Hannay C, Williamson DL, Hack JJ, Kiehl JT, Olson JG, Klein SA, Bretherton CS, Köhler M. 2009. Evaluation of forecasted southeast Pacific stratocumulus in the NCAR, GFDL, and ECMWF Models. *J. Clim.* **22**: 2871–2889.
Hoskins BJ, Karoly DJ. 1981. The steady linear response of a spherical atmosphere to thermal and orographic forcing. *J. Atmos. Sci.* **38**: 1179–1196.
Insel N, Poulsen CJ, Ehlers TA. 2010. Influence of the Andes Mountains on South America moisture, transport, convection and precipitation. *Clim. Dyn.* **35**(7–8): 1477–1492.
Jones C. 2015. The Madden–Julian Oscillation and boreal winter forecast skill: an analysis of NCEP CFSv2 reforecasts. *J. Clim.* **28**: 6297–6307.
Jones C, Carvalho L. 2002. Active and break phases in the South American Monsoon System. *J. Clim.* **15**: 905–914.
Juliá C, Rahn DA, Rutllant JA. 2012. Assessing the influence of the MJO on strong precipitation events in subtropical, semi-arid north-central Chile (30°S). *J. Clim.* **25**: 7003–7013.
Kerber F, Querel RR, Rondanelli R, Hanuschik R, van den Ancker M, Cuevas O, Smette A, Smoker J, Rose T, Czekala H. 2014. An episode of extremely low precipitable water vapour over Paranal observatory. *Mon. Not. R. Astron. Soc.* **439**: 247–255.
Kim H-M, Webster PJ, Toma VE, Kim D. 2014. Predictability and prediction skill of the MJO in two operational forecasting systems. *J. Clim.* **27**: 5364–5378.
Kobayashi S, Ota Y, Harada Y, Ebita A, Moriya M, Onoda H, Onogi K, Kamahori H, Kobayashi C, Endo H, Miyaoka K, Takahashi K. 2015. The JRA-55 reanalysis: general specifications and basic characteristics. *J. Meteorol. Soc. Jpn.* **93**: 5–48.
Lenters J, Cook K. 1995. Simulation and diagnosis of the regional summertime precipitation climatology of South America. *J. Clim.* **8**: 2988–3005.
Madden RA, Julian PR. 1971. Detection of a 40–50 day oscillation in the zonal wind in the tropical Pacific. *J. Atmos. Sci.* **28**: 702–708.
Madden RA, Julian PR. 1972. Description of global-scale circulation cells in the Tropics with a 40–50 day period. *J. Atmos. Sci.* **29**: 1109–1123.
Madden RA, Julian PR. 1994. Observations of the 40–50 day tropical oscillation – a review. *Mon. Weather Rev.* **122**: 814–837.
Marín JC, Pozo D, Mlawer E, Turner DD, Curé M. 2013. Dynamics of local circulations in mountainous terrain during the RHUBC-II project. *Mon. Weather Rev.* **141**: 3641–3656.
Marín JC, Pozo D, Curé M. 2015. Estimating and forecasting the precipitable water vapor from GOES satellite data at high altitude sites. *Astron. Astrophys.* **573**: A41.
Mechoso CR, Farrara JD, Ghil M. 1991. Intraseasonal variability of the winter circulation in the Southern Hemisphere atmosphere. *J. Atmos. Sci.* **48**: 1387–1404.
Miyakawa T, Satoh M, Miura H, Tomita H, Yashiro H, Noda AT, Yamada Y, Komada C, Kimoto M, Yoneyama K. 2014. Madden–Julian Oscillation prediction skill of a new-generation global model demonstrated using a supercomputer. *Nat. Commun.* **5**: 1–6.
Navarro-González R, Rainey FA, Molina P, Bagaley DR, Hollen BJ, de la Rosa J, Small AM, Quinn RC, Grunthaner FJ, Cáceres L, Gomez-Silva B, McKay CP. 2003. Mars-like soils in the Atacama Desert, Chile, and the dry limit of microbial life. *Science* **302**: 1018–1021.
Pardo JR, Cernicharo J, Lellouch E, Paubert G. 1996. Ground-based measurements of middle atmospheric water vapor at 183 GHz. *J. Geophys. Res.* **101**(D22): 28723–28730.
Peterson JB, Radford SJE, Ade PAR, Chamberlin RA, OKelly MJ, Peterson KM, Schartman E. 2003. Stability of the submillimeter brightness of the atmosphere above Mauna Kea, Chajnantor, and the South Pole. *Publ. Astron. Soc. Pac.* **115**(805): 383–388.
Radford SJE. 2011. Observing conditions for submillimeter astronomy. *Revista Mexicana de Astronomia y Astrofísica, Serie de Conferencias* **41**: 87–90.
Rashid HA, Hendon HH, Wheeler MC, Alves O. 2011. Prediction of the Madden–Julian Oscillation with the POAMA dynamical prediction system. *Clim. Dyn.* **36**: 649.
Ricaud P, Gabard B, Derrien S, Chaboureau J-P, Rose T, Monbauer A, Czekala H. 2010. HAMSTRAD-Tropo, a 183-GHz radiometer dedicated to sound tropospheric water vapor over Concordia Station, Antarctica. *IEEE Trans. Geosci.* **48**: 1365–1380.
Rodwell M, Hoskins B. 2001. Subtropical anticyclones and summer monsoons. *J. Clim.* **14**: 3192–3211.
Rondanelli R, Molina A, Falvey M. 2015. The Atacama surface solar maximum. *Bull. Am. Meteorol. Soc.* **96**: 405–418.
Rose T, Crewell S, Lohnert U, Simmer C. 2005. A network suitable microwave radiometer for operational monitoring of the cloudy atmosphere. *Atmos. Res.* **75**: 183–200.
Rutllant JA, Fuenzalida H, Aceituno P. 2003. Climate dynamics along the arid northern coast of Chile: the 1997–1998 Dinámica del Clima de la Región de Antofagasta (DICLIMA) experiment. *J. Geophys. Res.* **108**(D17): 4538.
Saha S, Moorthi S, Pan HL, Wu X, Wang J, Nadiga S, Tripp P, Kistler R, Woollen J, Behringer D, Liu H, Stokes D, Grumbine R, Gayno G, Wang J, Hou YT, Chuang HY, Juang HMH, Sela J, Iredell M, Treadon R, Kleist D, Van Delst P, Keyser D, Derber J, Ek M, Meng J, Wei H, Yang R, Lord S, Van Den Dool H, Kumar A, Wang W, Long C, Cheliah M, Xue Y, Huang B, Schemm JK, Ebisuzaki W, Lin R, Xie P, Chen M, Zhou S, Higgins W, Zou CZ, Liu Q, Chen Y, Han Y, Cucurull L, Reynolds RW, Rutledge G, Goldberg M. 2010. The NCEP climate forecast system reanalysis. *Bull. Am. Meteorol. Soc.* **91**: 1015–1057.
Sarazin M, Kerber F, de Breuck C. 2013. Precipitable water vapour at the ESO Observatories: the skill of the forecasts. *Messenger* **152**: 17–21.
Sardeshmukh PD, Hoskins BJ. 1988. The generation of global rotational flow by steady idealized tropical divergence. *J. Atmos. Sci.* **45**: 1228–1251.
Tremblin P, Schneider N, Minier V, Al Durand G, Urban J. 2012. Worldwide site comparison for submillimetre astronomy. *Astron. Astrophys.* **548**: A65.
Vuille M. 1999. Atmospheric circulation over the Bolivian Altiplano during dry and wet periods and extreme phases of the Southern Oscillation. *Int. J. Climatol.* **19**: 1579–1600.

Wang B. 2011. Multi-model ensemble forecast of MJO: progress of ISV Hindcast Experiment (ISVHE) and preliminary results. Climate Test Bed PI's Meeting, 6 October 2011, Fort Worth, TX, p. A3.

Wheeler MC, Hendon HH. 2004. An all-season realtime multivariate MJO index: development of an index for monitoring and prediction. *Mon. Weather Rev.* **132**: 1917–1932.

Wu J, Ren H-L, Zuo J, Zhao C, Chen L, Li Q. 2016. MJO prediction skill, predictability, and teleconnection impacts in the Beijing Climate Center Atmospheric Circulation Model. *Dyn. Atmos. Oceans* **75**: 78–90.

Xiang B, Zhao M, Jiang Z, Lin S-J, Li T, Fu X, Vecchi G. 2015. The 3-4-week MJO prediction skill in a GFDL coupled model. *J. Clim.* **28**: 5351–5364.

Zhang C. 2005. Madden–Julian Oscillation. *Rev. Geophys.* **43**: RG2003, doi: 10.1029/2004RG000158.

Zhang C. 2013. Madden–Julian Oscillation: bridging weather and climate. *Bull. Am. Meteorol. Soc.* **94**: 1849–1870.

